Hindawi
Wireless Communications and Mobile Computing
Volume 2017, Article ID 4313748, 15 pages
https://doi.org/10.1155/2017/4313748

WILEY | Hindawi

Research Article

In-Body Ranging with Ultra-Wideband Signals: Techniques and Modeling of the Ranging Error

Muzaffer Kanaan and Memduh Suveren

Department of Mechatronics Engineering, Faculty of Engineering, Erciyes University, Melikgazi, 38039 Kayseri, Turkey

Correspondence should be addressed to Muzaffer Kanaan; mkanaan@erciyes.edu.tr

Received 19 July 2016; Revised 18 October 2016; Accepted 31 October 2016; Published 15 January 2017

Academic Editor: Mauro Biagi

Results about the problem of accurate ranging within the human body using ultra-wideband signals are shown. The ability to accurately measure the range between a sensor implanted in the human body and an external receiver can make a number of new medical applications such as better wireless capsule endoscopy, next-generation microrobotic surgery systems, and targeted drug delivery systems possible. The contributions of this paper are twofold. First, we propose two novel range estimators: one based on an implementation of the so-called CLEAN algorithm for estimating channel profiles and another based on neural networks. Second, we develop models to describe the statistics of the ranging error for both types of estimators. Such models are important for the design and performance analysis of localization systems. It is shown that the ranging error in both cases follows a heavy-tail distribution known as the Generalized Extreme Value distribution. Our results also indicate that the estimator based on neural networks outperforms the CLEAN-based estimator, providing ranging errors better than or equal to 3.23 mm with 90% probability.

1. Introduction

The concept of a Body Area Network (BAN) is an emerging paradigm in medical information and communication technology (ICT) that has been steadily gaining popularity. The basic building blocks of a BAN are small, low-power sensors deployed inside, on, or even off the body surface, as shown in Figure 1. These devices can be used for sensing a wide variety of parameters associated with human health and wellness. Potential application domains for BANs are e-health, public safety/military, and even personalized entertainment [1]. Out of all these application domains, the case of implant communications where the sensors are implanted inside the human body is the focus of the current paper. Examples of such implant applications include wireless capsule endoscopy (WCE) [2], targeted drug delivery vehicles, and next-generation microrobotic surgery systems. For just about all these applications, knowing the location of an implant sensor (or robot) inside the body can be a critical piece of information. For example, in WCE-based disease diagnosis in the small intestine knowing the location where an image was taken could aid in more effective treatment of abnormal conditions (such as intestinal bleeding and tumors) [3]. Targeted drug delivery vehicles can result in more effective drug delivery to the diseased area, resulting in more effective treatment with less discomfort for cancer patients compared to currently used treatment modalities like chemotherapy. For this scenario, the location of the drug delivery vehicle is naturally of interest in order to make sure that the drug is delivered to the right area. Next-generation microrobotic surgery could revolutionize surgery, allowing medical procedures with minimal discomfort for patients, both during and after the procedure. This application example would also be impossible without knowledge of the location of the implanted microrobot within the body.

In general, the ability to localize a wireless transceiver can be solved by measuring various characteristics of the signal received from the transceiver at various *reference points* (whose locations are known with respect to some coordinate system). These characteristics of the signal, known as *location metrics*, are of three main types: Time of Arrival (TOA), Angle of Arrival (AOA), and Received Signal Strength (RSS) [4]. The measurements of these metrics are then processed with an appropriate algorithm to come up with

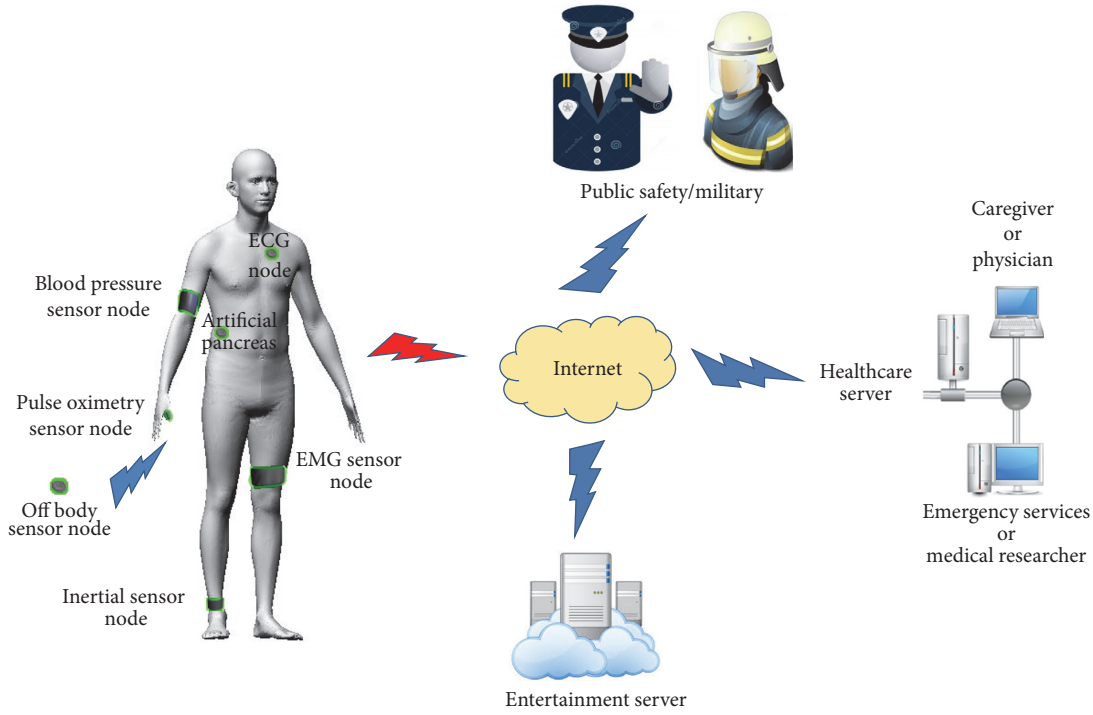

Figure 1: General structure of a Body Area Network (BAN).

a final location estimate. In challenging cases of practical importance (such as the indoor environment), AOA is not usable by itself for accurate location estimation, as in this case the line-of-sight (LOS) path between the transmitter and receiver is usually blocked, resulting in dramatically large errors in AOA estimation [4]. It is conceivable that a lossy, nonhomogeneous environment like the human body will be even more challenging for AOA estimation. Therefore, our focus in this paper will be on TOA and RSS metrics.

The measurements of both TOA and RSS can be used to come up with an estimate of the distance or *range* between the wireless transceiver to be located and a specific reference point. These range estimates are then used to come up with an estimate of the location. Therefore, the problem of determining the range, known as the *ranging problem* in the literature, is of fundamental importance in localization systems.

In recent years, Ultra-wideband (UWB) and Impulse Radio UWB (IR-UWB) in particular have been attracting attention for possible use in BAN applications. The advantages of UWB for these scenarios include simple transceiver architectures enabling low-power consumption (a critical requirement for implant applications and also for minimizing interference to other systems [5]) and wide bandwidth, resulting in communications at a higher data rate [6]. In fact, it is precisely for these reasons that UWB is being considered as the technology platform for next-generation WCE systems [7]. In addition, UWB systems are capable of high-accuracy ranging in challenging multipath environments, such as the indoor environment, where traditional localization systems such as GPS typically fail [8]. A localization system for an in-body application such as WCE will typically require millimeter-scale accuracy, which will in turn require high-quality range estimates. The objective of the study reported in this paper is to investigate the overall feasibility of high-accuracy in-body ranging using UWB signals.

With the above points in mind, it makes sense to pose the following questions. If UWB systems can be used successfully in challenging environments such as the indoor scenario, can they also be used for high-accuracy ranging in the in-body environment as well? And what kind of range estimators can be used for this purpose? Could millimeter-scale accuracy be obtained from these range estimators? The first contribution of the present paper is to address these questions. We do this by proposing two novel range estimators, one based on an implementation of the CLEAN algorithm [9] and another based on neural networks (NNs). Our results clearly demonstrate the feasibility of obtaining millimeter-scale ranging accuracy in the in-body environment, as will be apparent from the results in the later sections of the paper.

Besides the design of range estimators, another significant problem for high-accuracy in-body localization is that of *ranging error* (also known as *distance measurement error*). At the core of this problem is the physics of radio wave propagation inside the human body. The human body is an example of a geometrically complex, nonhomogeneous, lossy propagation environment, where the permittivity and conductivity of different body tissues are frequency-dependent [10]. As a result, different frequency components of a UWB signal are delayed and attenuated by different amounts, resulting in significant signal distortion at the receiver. The effects of the channel on the UWB signal are thus frequency-selective and highly nonlinear. Previous work on modeling the frequency-dependence of the channel characteristics can be found in [11–18] and a recent comprehensive study characterizing

the highly nonlinear nature of the frequency-selective in-body channel (including the frequency-dependence of the scattering phenomenon) can be found in [19].

For range estimation, the net result of this channel behavior is random, and sometimes large, values of ranging error. The effects of the human body on TOA-based ranging performance have been studied previously (see, e.g., [20–23]); however, these studies focused on the scenario of body-mounted sensors and are not readily applicable to the case of in-body ranging. There do not appear to be a lot of studies dealing with the issue of ranging in the in-body environment. In [24], characterization of the ranging error is undertaken at the MICS band (402–405 MHz), which is the band currently used for implant BAN applications. Ranging performance in both the UWB and narrowband (i.e., MICS band) cases is compared in [25, 26]; this comparison was based on a homogeneous approximation of the in-body environment. An analysis of maximum likelihood techniques for UWB-based in-body ranging based on previously proposed implant propagation models was undertaken in [27]; this study highlighted both the challenges associated with the in-body environment and the resulting poor performance of this well-known estimator. It is clear, therefore, that more analysis is necessary in order to really understand the behavior of the ranging error in the in-body environment with UWB signaling, given the highly nonhomogeneous nature of the propagation environment inside the human body. An analysis of the ranging error, therefore, is also undertaken and forms the second contribution of the present paper.

The rest of this paper is organized as follows. In Section 2, we review the fundamental problems of in-body ranging using UWB signals and outline the concepts of the two range estimators. Section 3 presents the framework for performance evaluation of the two estimators proposed. The performance of both estimators are presented and compared in Section 4. Section 5 concludes the paper.

2. In-Body Ranging with Ultra-Wideband Signals

In this section, we propose and present the details of two techniques for ranging using UWB signals in the in-body environment, one based on an implementation of the CLEAN algorithm [9] and another based on neural networks.

2.1. Ranging with the CLEAN Algorithm. The CLEAN algorithm has been used in previous studies in order to extract the multipath characteristics of radio propagation for cases such as the indoor scenario [28]. In this study, the CLEAN algorithm is used to derive the channel profile for the in-body environment and estimate the TOA for ranging. To set the stage for this discussion, recall that traditional TOA-based ranging uses the one-way propagation delay (Δt), also known as the TOA, in order to estimate the range (or distance), d_0, between a transmitter and a receiver as given by the equation

$$d_0 = c \times \Delta t, \tag{1}$$

where c is the speed of light in free space. Since the speed of light in free space is constant, an accurate estimate of Δt is sufficient in order to come up with a precise estimate of the range. When trying to estimate the range between an implanted sensor and a receiver located at a distance, d, above the body surface, the different relative permittivity values of various body tissues imply that (1) needs to be modified as

$$d_0 = \frac{c}{\sqrt{\varepsilon_r}} \times \Delta t, \tag{2}$$

where ε_r represents the relative permittivity of the tissue that the signal is going through. Substantially, (2) implies that large ranging errors are possible because of the nonhomogeneous nature of the in-body environment, since the speed of light changes within the different types of tissue. Therefore, simply estimating the TOA accurately is no longer sufficient for accurate range estimation; a mathematical model of the variation of ε_r is also necessary in order to estimate the signal propagation speed within the different tissues.

The structure of the CLEAN algorithm is shown in the flowchart of Figure 2 and is well documented in the literature. The general idea is to find the largest pulse embedded within

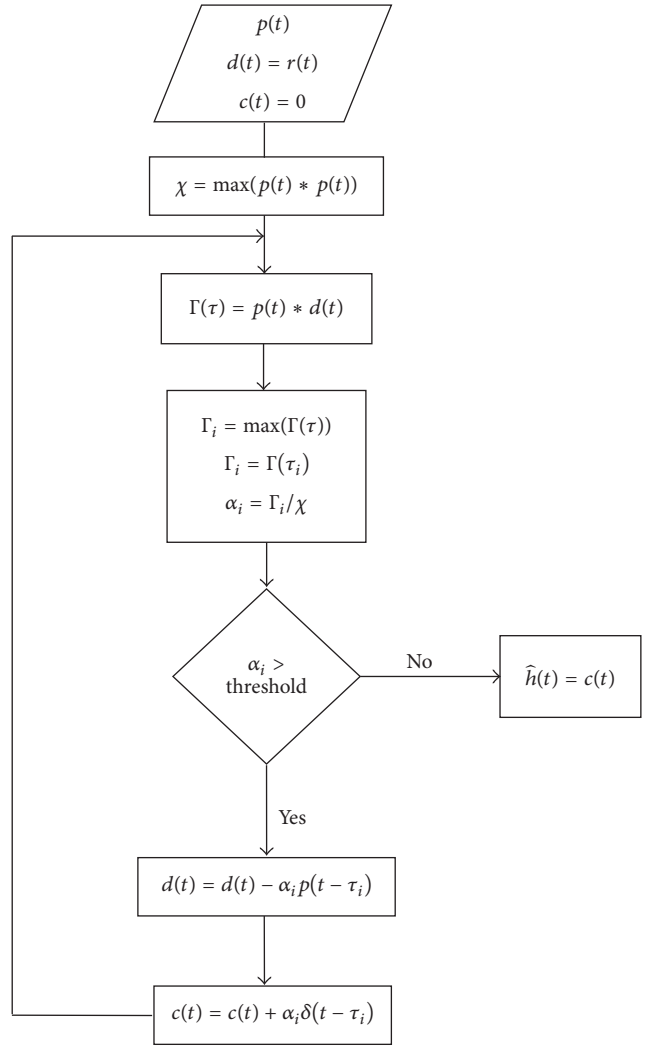

Figure 2: Structure of the CLEAN algorithm.

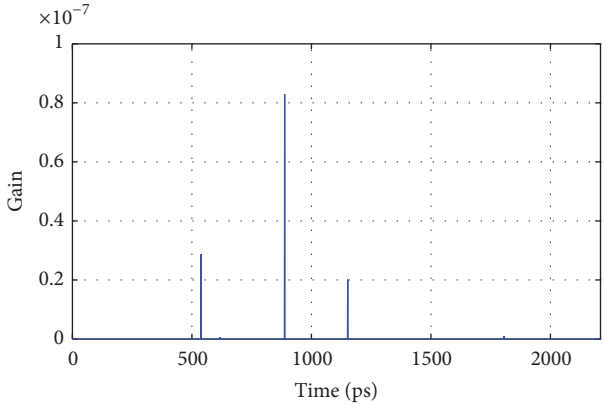

Figure 3: Sample channel profile produced by the CLEAN algorithm.

the received signal, $d(t)$, by correlating it with a template signal, $p(t)$, that is specified in advance [29]. For the purposes of this study, this template signal was the UWB pulse applied at the antenna input (more details on this template signal are given in Section 3). The power contribution for this largest pulse is then subtracted from the original signal, thereby removing its impact. The amplitude, Γ_i, and time delay, τ_i, of this largest pulse are then used to add an impulse to the channel profile (denoted by $c(t)$ in Figure 2) with a time delay, τ_i, and a normalized amplitude, α_i, as given by

$$\alpha_i = \frac{\Gamma_i}{\chi}, \tag{3}$$

where χ is the maximum value of the autocorrelation function of $p(t)$; that is,

$$\chi = \max\left(p(t) \otimes p(t)\right) \tag{4}$$

and "⊗" denotes the correlation operator. As seen in Figure 2, this whole process is repeated until the value of α_i falls below a certain threshold value which, in this study, has been taken to be 10% of the amplitude of the largest pulse. The end result of the algorithm is a channel profile that consists of a series of impulses, as seen in Figure 3.

From the channel profile, an estimate of the propagation time delay, Δt, is determined. The next phase of ranging involves an estimation of the ε_r value for the path the signal traveled over. Normally, this step is complicated by the nonhomogeneous nature of the human body and the fact that the thickness of each tissue is different (which implies that their contribution to the overall ε_r value will change). However, it is possible to circumvent this difficulty and come up with an average ε_r value with respect to this nonhomogeneous environment, as discussed next.

For a given path between the transmitter to the receiver and known actual distance, d_0, (2) can be rearranged to give

$$\varepsilon_r = \left(\frac{c}{d_0} \times \Delta t\right)^2 \tag{5}$$

and thus (5) can be used to estimate the value of ε_r as a function of the implant depth, namely, $\varepsilon_r(d_0)$. This could

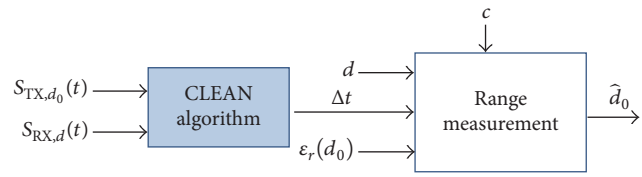

Figure 4: General structure of the CLEAN-based range estimator. $S_{TX,d_0}(t)$ and $S_{RX,d}(t)$ represent the transmitted and received signals associated with an implant sensor at depth d_0, respectively.

be accomplished by first obtaining a series of ε_r values for different known values of d_0 and then characterizing the functional dependence of ε_r on d_0 by means of curve-fitting (this point is further discussed in Section 3). Assuming the general case that the receiving antenna is located d mm away from the body surface, an estimate of the implant depth beneath the body surface, $\widehat{d}_0$, could be calculated as

$$\widehat{d}_0 = \min_{\forall d_0}\left(\left|d_0 - d_{0,\text{est}}\right|\right) = \min_{\forall d_0}\left(\left|d_0 - v_{\text{body}} \cdot t_{\text{body}}\right|\right), \tag{6}$$

where $v_{\text{body}} = c/\sqrt{\varepsilon_r}$ is the speed of propagation inside the body tissues and

$$t_{\text{body}} = \Delta t - \frac{d}{c} \tag{7}$$

is the net amount of time delay due to body tissues. In calculating this value, we use the fact that the receiving antenna is located at a distance, d, above the body surface. Over this distance, the signal would travel at the normal speed of light in free space, incurring a delay equal to d/c. This value is then subtracted from the total TOA derived from the channel profile, Δt, to give the total amount of time delay *due to body tissues only*. The estimator for d_0 can then be expressed as

$$\widehat{d}_0 = \min_{\forall d_0}\left(\left|d_0 - \frac{c}{\sqrt{\varepsilon_r(d_0)}}\left(\Delta t - \frac{d}{c}\right)\right|\right). \tag{8}$$

In summary, the ranging process with the CLEAN algorithm consists of two phases. In the first phase, the received signal is used to determine the channel profile, which is used to determine the TOA. The estimated TOA values are then used to come up with a mathematical model of the variation of the relative permittivity, namely, $\varepsilon_r(d_0)$. Finally, based on these two pieces of information, an estimate of the implant depth, $\widehat{d}_0$, is obtained using (8). The full structure of the CLEAN-based range estimator is shown in Figure 4.

We are now in a good position to comment on the practical feasibility of the CLEAN-based estimator. As discussed above, this estimator requires "template" channel profiles for different combinations of transmitter and receiver antenna positions in order to come up with estimates of the TOA and relative permittivity. As discussed previously, the human body is an inhomogeneous environment composed of different tissue types which exhibit frequency-dependent electrical characteristics. In addition, no two human bodies

are exactly alike. Therefore, obtaining this information could be computationally challenging. Nevertheless, it is possible to get this information by running the algorithms on the body model data obtained from an individual patient (e.g., through 3D reconstruction from MR images [30]). This could increase the computational load, a disadvantage if the ranging needs to be performed on a near-real-time basis (for microrobotic surgery applications, e.g.). However, for some applications such as the WCE systems currently used in clinical practice, ranging and localization calculations could all be performed offline as part of the normal data postprocessing (since the ranging and localization data does not need to be known on a real-time basis), thereby rendering this approach practically feasible.

The above-mentioned procedure for the CLEAN-based estimator requires that we have an accurate characterization of the average ε_r value for many different values of the implant depth d_0. This can be accomplished computationally by embedding the transmit antenna at different known depths (within the 3D model acquired from the actual patient as discussed in the previous paragraph), determining the average ε_r value for each value of d_0 and then employing curve-fitting to generalize the results and obtain a closed-form expression to characterize the dependency of ε_r on d_0. Obviously, this characterization will be more accurate as we obtain values of ε_r for many different values of d_0. This has an advantage in the sense that more accurate ranging is possible with the CLEAN-based estimator. The disadvantage is that the computational load associated with the CLEAN-based estimator will be increased.

One final comment with regard to ranging with the CLEAN algorithm is described in the following. Since the CLEAN algorithm operates in the time domain, the ranging method with the CLEAN algorithm is inherently a time domain method. This fact allows it to be distinguished from the ranging method using NN techniques, which is a frequency-domain method, as will be clear from the discussion in the next subsection.

2.2. Ranging with Neural Network (NN) Techniques. Contrary to ranging with the CLEAN algorithm, which uses the TOA metric to estimate the range, the ranging method with NNs uses the RSS metric. Before presenting the details of this estimator, however, the following question needs to be addressed: why a machine-learning technique, such as a neural network, when there are so many other range estimators is proposed in the open literature?

To the best of our knowledge, most of the UWB-based range estimators proposed in the open literature are based on TOA estimation (e.g., see [31–33]). The wide bandwidth of UWB signals allows an accurate estimation of the TOA even in challenging multipath scenarios (such as the indoor setting, e.g.). However, accurate estimate of the TOA within the body is complicated by the fact that the human body is a lossy, nonhomogeneous medium with frequency-dependent conductivity and permittivity characteristics for the different tissues. This inevitably leads to the observation that it is more feasible to use RSS, rather than TOA, for the ranging process within the body. As previously observed by other researchers, RSS-based ranging and localization problems are more amenable to machine-learning techniques, such as neural networks [34–37]. This is the main reason behind the use of the NN-based range estimator in this study.

To motivate the development of the NN-based range estimator, we present the familiar path loss expression between a transmitter and a receiver located a distance d apart, as given by

$$\mathrm{PL}_{\mathrm{dB}} = \mathrm{PL}_0 + 10 \cdot n \cdot \log_{10}\left(\frac{d}{d_0}\right), \tag{9}$$

where $\mathrm{PL}_{\mathrm{dB}}$ represents the path loss in dB, PL_0 is the path loss value at a reference distance from the transmitter, d_0 is the implant depth from the body surface (i.e., the distance between the transmit antenna within the body and the body surface), and n is the path loss exponent. The value of n is dependent on the specific environment where the radio waves propagate. It is possible to use (9) to estimate the range between the implant sensor and the receiver. However, because of the fact that the human body is a lossy medium, the values of n can differ greatly between different tissue types. In addition, given the wide bandwidth of UWB signals, n is dependent on frequency as well [19]. All this complicates the process of in-body ranging using RSS inside the body.

NNs can be leveraged to solve this problem in the following way. First, Finite Difference Time Domain (FDTD) simulation results at known values of the implant depth are used to obtain the magnitude of the Poynting vector data at distances on and off the body surface, after a UWB signal is applied at the input of the implanted sensor antenna. The Poynting vector is defined as the vector product

$$\mathbf{S}(t) = \mathbf{E}(t) \times \mathbf{H}(t), \tag{10}$$

where $\mathbf{E}(t)$ and $\mathbf{H}(t)$ are the values of the electric and magnetic field intensities, respectively. The magnitude values of the Poynting vector are then subjected to a Fast Fourier Transform (FFT) operation to obtain the values of the Poynting vector at discrete frequency values. This operation, in essence, allows us to take into account the frequency-dependence of the path loss into account as part of the ranging process. The resulting FFT sequence is then downsampled to reduce the data size. The reason for this step is that both the training time and RAM requirements for training the neural network are both influenced by the size of the input data, so this downsampling step is performed to keep these parameters within tolerable limits. These Poynting vector values are dependent on the implant depth, d_0, as well as the distance of the receiving antenna above the body surface, d. These values are then used to train a neural network in a supervised manner. The general structure of the NN-based estimator is depicted in Figure 5.

Once the training process is complete, the network could be used to estimate the implant depth, given a sequence of values of the Poynting vector data at different frequencies and a given distance d for the receiving antenna above the body surface. For the purposes of this study, three NN structures were considered: the classic multilayer perceptron (MLP), a variant known as Cascade-MLP (C-MLP) and the

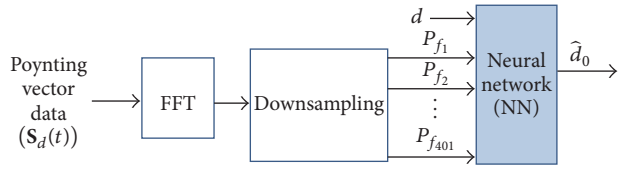

Figure 5: The general structure of the NN-based range estimator ($\mathbf{S}_d(t)$ represents the time-dependent Poynting vector data at a distance d from the body surface).

Elman network. The details of these three structures will be discussed in the next section.

Regarding the practical feasibility of the NN-based estimator, the same kinds of issues with respect to individuality of different human bodies and the inhomogeneous nature of the in-body environment exist, just as in the CLEAN-based estimator. However, as discussed in the previous section on the CLEAN-based estimator, it is possible to somewhat circumvent these issues by running the proposed NN algorithms on the real 3D body models obtained from individual patients. Again, the computational load could potentially be high but could be manageable for applications where the ranging data does not need to be known on a real-time basis.

For the NN-based estimator to work, it is necessary to first characterize the dependence of the Poynting vector values on the implant depth, d_0, as well as frequency. As with the CLEAN-based estimator, this process can be performed computationally by embedding the transmit antenna at a known implant depth within the 3D model acquired from the actual patient and then calculating the required Poynting vector values from FDTD simulations. The advantage of this approach is that it could result in more accurate ranging performance compared to the CLEAN-based estimator (as will be clear from the results presented in Section 4); however, the computational load could be increased.

3. Performance Analysis Framework

In order to assess the performance of the different range estimators, the first requirement is a 3D voxel model of the human body. For the purposes of this study, a 3D model, developed by the US National Library of Medicine under the name of the Visible Human Project (VHP) data set, was utilized [37]. Of course, there are alternatives to the VHP data set; however, this data set was the only one compatible with the modeling software used at the time this study was performed. The data set was incorporated into the XFDTD™ software, which is a 3D electromagnetic simulation platform using the FDTD method to calculate the electric and magnetic field intensities over any region of space, given the material properties and boundary conditions [38]. The full-body voxel model is shown in Figure 6(a).

Since FDTD calculations can be computationally intensive, the 3D voxel model was constrained by truncating it until only the region around the chest remained, as can be seen in Figure 6(b). This truncation can be intuitively justified by keeping in mind that the human bodyis a lossy environment; therefore, the radiation from an antenna placed inside the body will be confined to the general vicinity of the antenna. More details on the antenna placement will be given later in this section.

A cell size value of 2 mm in the x and y directions and 0.5 mm in the z direction was used for the FDTD calculations in order to satisfy the Courant limit. The Perfectly Matched Layer (PML) boundary condition was applied to the simulation scenario in order to be able to discard the effects of reflections from the body environment.

After the voxel body model was set up, a UWB antenna was defined in the software and placed inside the model. The antenna used was the elliptic disc dipole antenna [39], shown in Figure 7(a). The antenna location selected was the chest region, approximately at the same level as the heart, as seen in Figure 7(b). With the antenna center point as the reference, the antenna was placed at a depth, d_0, from the body surface. The input signal to the antenna (which was used as the template pulse for the CLEAN algorithm later on) was a modulated Gaussian pulse with a −10 dB bandwidth of 1.4 GHz and a center frequency of 4.1 GHz. The choice of these parameters restricted the spectral content of the signal to the 2–6 GHz interval, with most of the content in the 3.4–4.8 GHz range. The part of the UWB spectrum between 3.4 and 4.8 GHz is commonly referred to as the "UWB Low Band" in the literature [40]. Only this part of the UWB spectrum is considered in this study, given other previous studies reporting that UWB signals in this frequency range are able to better penetrate body tissues [41]. The power level at the antenna input was set to a value of 1 mW, using a 50 Ω source, and the antenna was fed from the feed point between the two elliptical discs [19]. It should be noted that the elliptic disc dipole antenna is just one example of a UWB antenna designed for implant applications and that the effects of antenna size as well as other antenna parameters on ranging performance are outside the scope of the study.

For the purposes of this study, d_0 values in the 40–60 mm range were considered (in 2 mm steps, with a total of 11 values). For each value of d_0 considered, Poynting vector magnitudes at designated observation points on and radially away from the body surface were considered. Each such point was characterized by a value of d/d_0, d being the absolute distance of the point above the body surface. There were 80 such points in the range $1 \leq d/d_0 \leq 5$. The Poynting vector data was logged and normalized to the power level at the antenna input 1 mW, and a value of the path loss with units of dBmW/m^2 was obtained. The data was then subjected to further processing, depending on the range estimation technique used. It should be noted at this juncture that the term "range" for the purposes of this study is defined to be the measured distance between the center point of the antenna and a point on the body surface.

For the CLEAN-based range estimator, the Poynting vector data was first processed with the CLEAN algorithm to come up with the channel profile. The TOA was estimated from the channel profile and the average value of ε_r was derived for each value of d_0 considered. In order to derive a mathematical model for $\varepsilon_r(d_0)$, curve-fitting was performed using a number of nonlinear functions. The best Root Mean

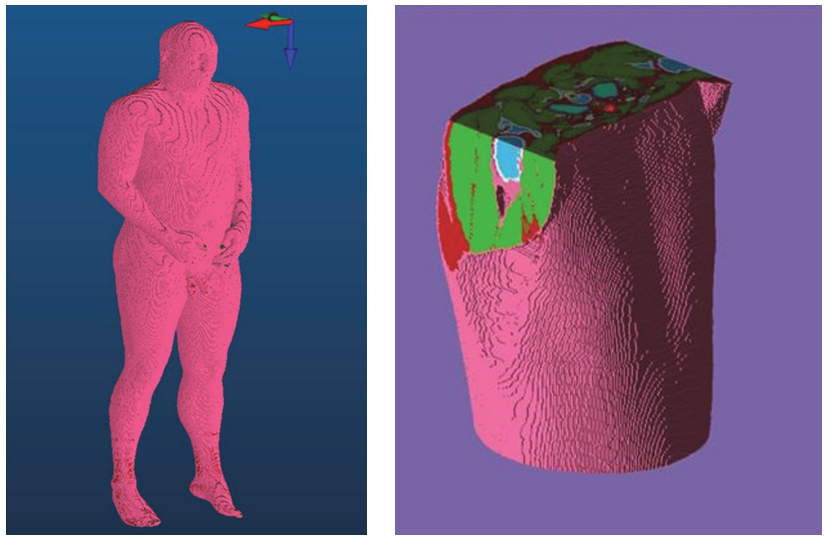

(a) (b)

Figure 6: 3D voxel models: (a) full-body model and (b) truncated model used for this study.

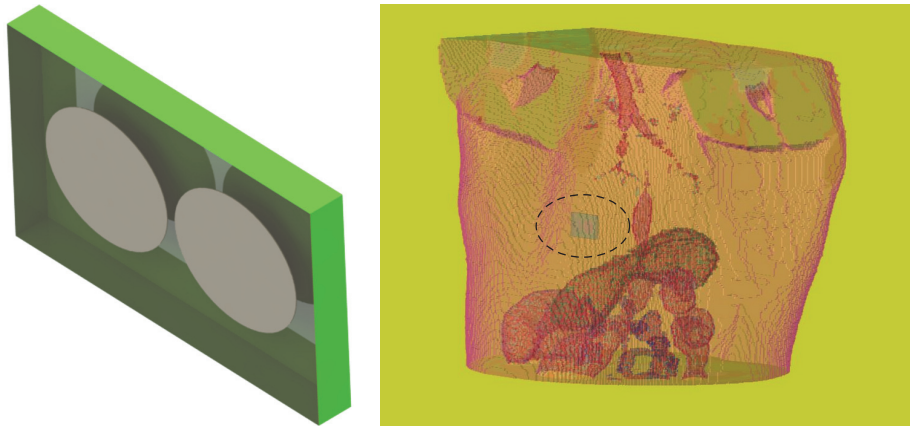

(a) (b)

Figure 7: (a) 3D view of the elliptic disc dipole antenna; (b) antenna placement within the 3D voxel model (the antenna location shown by the black oval).

Square Error (RMSE) performance was obtained with the *sum of sines* form expressed as

$$\begin{aligned}\varepsilon_r(d_0) &= 69.7\sin(0.0134d_0 + 5.88)\\ &\quad + 6.76\sin(0.423d_0 - 3.74)\\ &\quad + 4.06\sin(0.856d_0 + 4.75).\end{aligned} \tag{11}$$

The ε_r values derived for each value of d_0 as well as the nonlinear fit to the data (in the form of (11)) are shown in Figure 8.

For the NN-based range estimator, the FFT of the Poynting vector data was first computed. The FFT values at 401 discrete frequency values, together with the distance, d, were the inputs to the neural network. As stated in Section 2.2, three NN structures were considered for this study. For all three cases, there were a total of N inputs to the network. For this study, there were $N = 402$ inputs to each NN structure, as given by $r_i \in \mathbf{R} = \{d, P_{f_1}, P_{f_2}, \ldots, P_{f_{401}}\}$, where P_{f_i} $(i = 1, \ldots, 401)$ represents the Poynting vector magnitude at each of the 401 discrete frequencies, consisting of the 80 spatial points, each for a different value of d/d_0.

In order to enable an objective performance comparison among the three structures, certain parameters were kept the same. These common parameters are as follows:

(i) *The number of neurons in the hidden layer (denoted by M)* is 25.

(ii) *Activation function*: the activation function for all neurons in all structures was set to the tangent-sigmoid function, expressed as

$$\psi(x) = \frac{2}{1 + e^{-2x}} - 1. \tag{12}$$

(iii) *Learning algorithm*: it is Levenberg-Marquardt.

The input-output relationships for all three structures are given below.

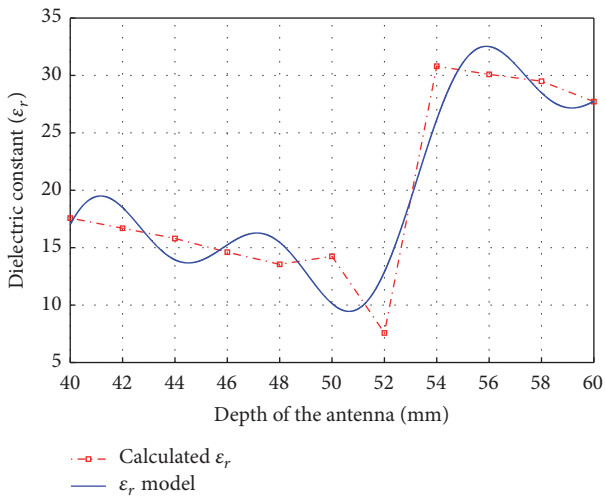

FIGURE 8: ε_r values as a function of d_0 (actual values and the fitted nonlinear model).

MLP Structure. Referring to Figure 9, the output of neuron j in the hidden layer (where $j = 1, \ldots, M$) can be written as

$$m_j = \psi\left(\sum_{i=1}^{N} w_{ij} r_i\right), \tag{13}$$

where w_{ij} represents the value of the synaptic weight associated with the connection from input i to neuron j. The final output of the network, denoted by $\widehat{d}_{0,\mathrm{MLP}}$, is

$$\widehat{d}_{0,\mathrm{MLP}} = \psi\left(\sum_{j=1}^{M} \beta_j m_j\right) \tag{14}$$

with β_j representing the value of the synaptic weight associated with the connection from neuron j to the output neuron.

Cascade-MLP (C-MLP) Structure. From Figure 10, we see that the C-MLP structure resembles the normal MLP structure, except that there is now a direct feedforward connection from the input layer to the output layer. The output of neuron j in the hidden layer is given by (13). The output of the network, denoted by $\widehat{d}_{0,\mathrm{CMLP}}$, is given by

$$\widehat{d}_{0,\mathrm{CMLP}} = \psi\left(\sum_{j=1}^{M} \alpha_j m_j + \sum_{i=1}^{N} \lambda_i r_i\right), \tag{15}$$

where α_j is the value of the synaptic weight associated with the connection from neuron j in the hidden layer to the output neuron and λ_i is the value of the synaptic weight associated with the connection from input i to the output layer.

Elman Structure. The Elman structure is a bit different from the MLP and C-MLP structures, as can be seen from Figure 11, in that it incorporates feedback from the output of the hidden layer back on to its input after traversing what is known as a *context layer* [42]. This structure was selected in order to see

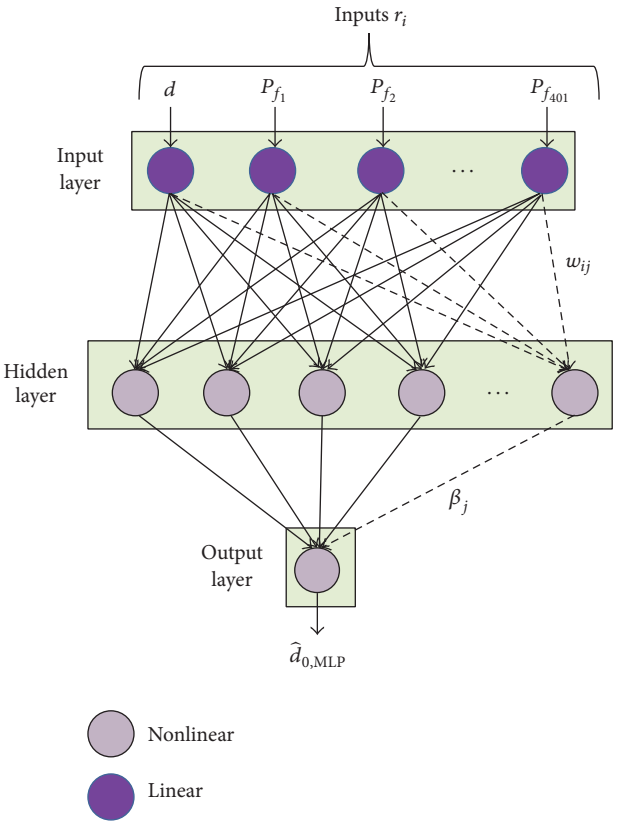

FIGURE 9: MLP network structure.

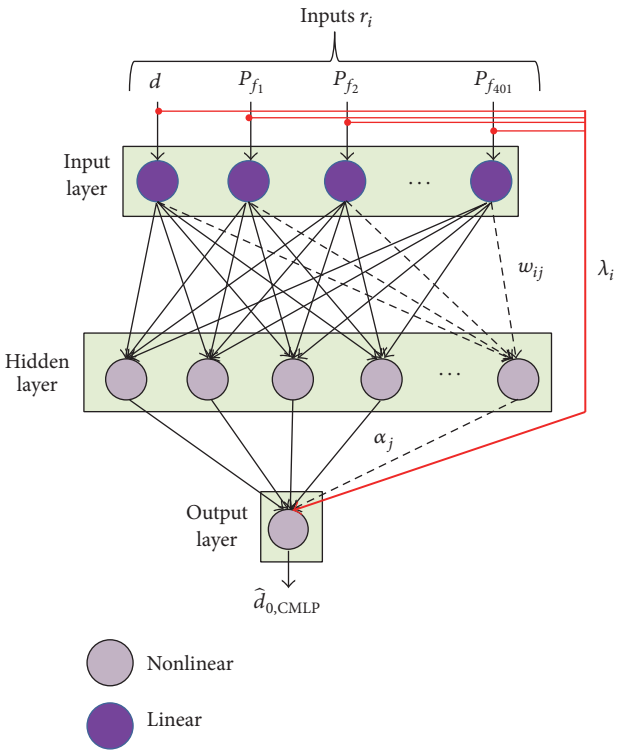

FIGURE 10: C-MLP network structure.

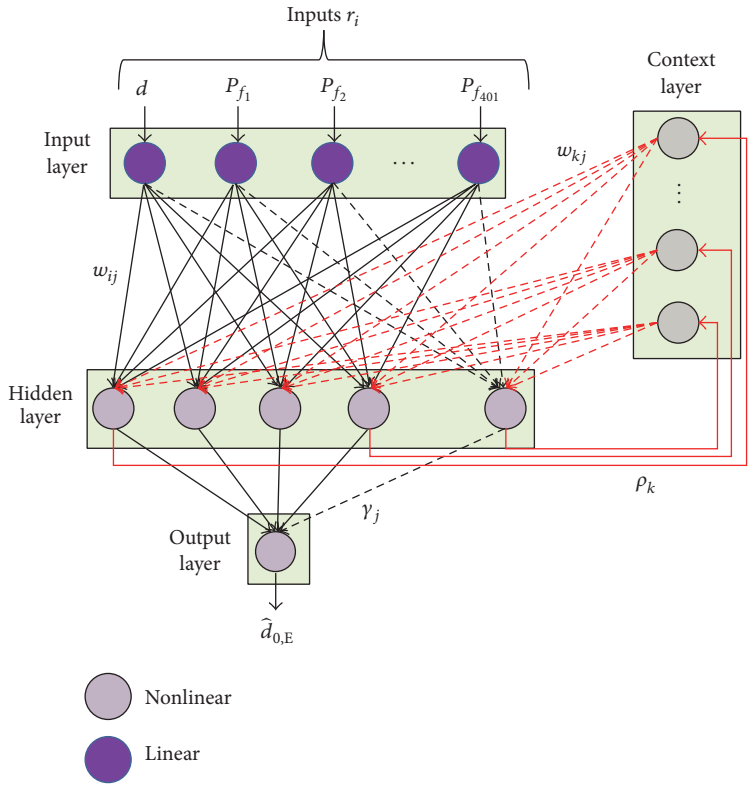

Figure 11: Elman network structure.

whether the feedback results in better range estimation. For the sake of simplicity, the number of neurons in the hidden and context layers was set to the same value (M).

In this case, the output of neuron j in the hidden layer is now given by

$$m_j = \psi\left(\sum_{i=1}^{N} w_{ij} r_i + \sum_{k=1}^{M} w_{kj} v_k\right), \tag{16}$$

where v_k is the output of neuron k ($k = 1, 2, \ldots, M$) in the context layer given by

$$v_k = \psi\left(\rho_k m_k\right) \tag{17}$$

and ρ_k is the value of the synaptic weight based on the connection from the output of neuron k in the hidden layer on to the context layer. The final output of the network, denoted by $\widehat{d}_{0,E}$, is given by

$$\widehat{d}_{0,E} = \psi\left(\sum_{j=1}^{M} \gamma_j m_j\right), \tag{18}$$

where γ_j is the value of the weight associated with the synaptic connection from neuron j to the output layer.

4. Results and Discussion

4.1. Results for the CLEAN-Based Range Estimator. In estimating the time delay, Δt, that forms the basis for range estimation, the time delay corresponding to the strongest path in the channel profile was used, as that gave a more accurate estimate of the range than the first arriving path. This is illustrated in the Root Mean Square Error (RMSE) figures of Table 1. Conventional wisdom holds that since the shortest path between any two points is a straight line, the signal on the direct path (DP) between the transmitter and receiver should suffer less delay and therefore get to the receiver first. While there are different techniques proposed in the literature for the estimation of the TOA [8], the TOA of the DP is considered to be important for challenging localization applications (such as indoor localization [4]) and the first detected signal above the receiver sensitivity threshold is generally accepted to be the TOA of the DP signal.

One possible explanation for this finding can be provided by the concept of *direct path (DP) excess delay*. It is known that a piece of material with thickness, d_m, and relative permittivity, $\varepsilon_{r,m}$, between the transmitter and the receiver introduces an excess delay to the DP signal Δt_E given by [8, 43, 44].

$$\Delta t_E = \left(\sqrt{\varepsilon_{r,m}} - 1\right)\frac{d_m}{c}. \tag{19}$$

The human body is a geometrically complex, highly non-homogeneous environment where different tissues can have very different permittivity values. Therefore, it is possible that range estimates in the in-body environment will be significantly affected by DP excess delay, since each tissue type encountered by the transmitted signal will add its own delay. In addition, since $\varepsilon_{r,m}$ is, in general, a function of frequency, it follows that Δt_E is also a function of frequency, meaning that different frequency components in the transmitted signal

Table 1: Comparison of the ranging error (RMSE) based on the strongest path versus the first arriving path.

d_0 (mm)	RMSE based on strongest path (mm)	RMSE based on first arriving path (mm)
40 mm	14,27	21,33
42 mm	5,63	11,76
44 mm	5,15	7,14
46 mm	3,83	8,13
48 mm	2,60	5,36
50 mm	3,43	10,11
52 mm	4,61	9,24
54 mm	2,25	8,00
56 mm	3,36	6,69
58 mm	7,87	6,48
60 mm	3,53	7,81

will be subjected to different amounts of delay. The general takeaway from all this is that for the in-body environment the DP signal may not get to the antenna first; in fact it is possible that it will be subjected to more delay than signals arriving via the other paths.

The ranging error is defined by

$$\zeta = \left| d_0 - \widehat{d}_0 \right|. \tag{20}$$

For the CLEAN-based range estimator, the ranging error has been characterized by the RMSE as a function of the implant depth and is given in Table 1.

As for the statistics of the ranging error, the empirical CDF of the ranging error was obtained and compared against a number of candidate distributions. The standard procedure in these cases is to measure the goodness-of-fit between the empirical CDF and the candidate distribution by means of hypothesis tests. In this study, the *Anderson-Darling (A-D) test,* implemented in MATLAB, was used with a significance level of 5% [45]. The test also calculates the p values [46]. If the value of p for a given candidate distribution exceeds the significance level, the test indicates that that distribution represents the ranging error data set. The empirical CDF was compared against nine candidate distributions in this manner. A sample of the ranging error data for illustrative purposes is shown in Figure 12, and the results of the A-D test with respect to all candidate distributions are given in Table 2.

From Table 2, it is seen that for most implant depths, the values of p are highest for the Generalized Extreme Value (GEV) distribution, indicating that it is a better representative for the empirical CDF of the ranging error than the others. The probability density function characterizing the GEV distribution is generally expressed as

$$f(x \mid \kappa, \mu, \sigma) = \left(\frac{1}{\sigma}\right) \cdot \exp\left(-\left(1 + \kappa\frac{(x-\mu)}{\sigma}\right)^{-1/\kappa}\right) \cdot \left(1 + \kappa\frac{(x-\mu)}{\sigma}\right)^{-1-1/\kappa}, \tag{21}$$

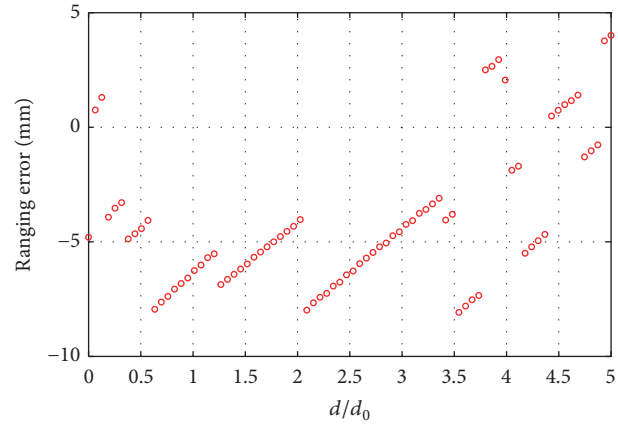

Figure 12: Sample results for the ranging error ($d_0 = 44$ mm).

where κ is the shape parameter for the distribution, μ is the location parameter, and σ is the scale parameter. Note that (21) holds for those cases where x and the three distribution parameters are such that the condition

$$\left(1 + \kappa\frac{(x-\mu)}{\sigma}\right) > 0 \tag{22}$$

is valid. The values of all three distribution parameters as a function of the implant depth are given in Table 3.

Finally, the CDF of the GEV distribution is plotted and compared against the empirical CDF of the ranging error data derived from the CLEAN algorithm, as depicted in Figure 13. Also shown for comparison purposes are the CDFs corresponding to lognormal and Weibull distributions. It can be clearly deduced from the figure that GEV is indeed the most appropriate distribution for modeling the errors resulting from the CLEAN-based range estimator.

4.2. Results for the NN-Based Range Estimator. The performance results for the three NN structures at the end of the training phase are presented in Table 4, where we clearly see that there is no significant difference with regard to the training time between the three networks. This is most likely due to the size of the input data set used for the training.

The performance of the three NN structures was compared in terms of the RMSE of the ranging error across all implant depths (d_0) considered, as shown in Table 5. An RMSE figure was computed for each value of d_0, and an average value of all the RMSE figures was also computed in order to have one figure of merit that can be used to compare all three networks. Based on these results, it is clear that the C-MLP structure has the best performance across all implant depths, followed by the Elman network and lastly the MLP structure. The performance edge of the C-MLP NN over the Elman structure is relatively minor (less than 4% across all implant depths); however, when one looks at the standard deviation of the RMSE across all implant depths (also presented in Table 5), the differences become more striking. It is clear that the C-MLP network can maintain a more consistent performance across all implant depths.

Table 2: The output of the A-D test (p values) as a function of d_0.

Distribution function	Antenna depth (mm)										
	40	42	44	46	48	50	52	54	56	58	60
Lognormal	0,05	0,01	0,00	0,00	0,03	0,47	0,12	0,05	0,09	0,09	0,01
Normal	0,63	0,14	0,50	0,62	0,19	0,00	0,01	0,53	0,21	0,00	0,08
GEV	1,00	0,21	0,83	0,40	0,41	0,81	0,86	0,76	0,30	0,41	0,40
Rayleigh	0,00	0,00	0,06	0,14	0,00	0,00	0,00	0,03	0,00	0,00	0,00
Weibull	0,91	0,04	0,13	0,49	0,51	0,65	0,71	0,69	0,48	0,45	0,64
Gamma	0,13	0,03	0,03	0,10	0,43	0,61	0,71	0,41	0,41	0,47	0,50
Exponential	0,00	0,01	0,00	0,00	0,34	0,58	0,35	0,02	0,07	0,44	0,48
Nakagami	0,27	0,08	0,09	0,30	0,93	0,16	0,40	0,91	0,70	0,30	0,87
Logistic	0,82	0,13	0,56	0,50	0,23	0,00	0,04	0,51	0,21	0,01	0,10

Table 3: Parameters of the GEV distribution as a function of the implant depth (d_0).

GEV parameters	Antenna depth (mm)										
	40	42	44	46	48	50	52	54	56	58	60
κ	−0,54	−0,45	−0,55	−0,46	0,14	0,56	0,29	−0,11	−0,05	0,45	0,22
σ	3,72	3,16	2,27	1,61	1,15	1,03	1,72	1,06	1,58	2,79	1,49
μ	13,10	3,97	4,27	3,12	1,23	1,01	1,93	1,38	1,92	2,71	1,58

Table 4: Comparison between the three NN structures on the basis of training time.

Network type	Number of the neurons in the hidden layer	Number of the neurons in the context layer	Number of epochs	Training time	Performance at the end of the training (MSE)
MLP	25	Not applicable	1000	8 hrs 19 min 04 sec	$2.12e-10$
C-MLP	25	Not applicable	1000	8 hrs 43 min 02 sec	$3.5e-10$
Elman	25	25	1000	9 hrs 01 min 39 sec	$9.14e-11$

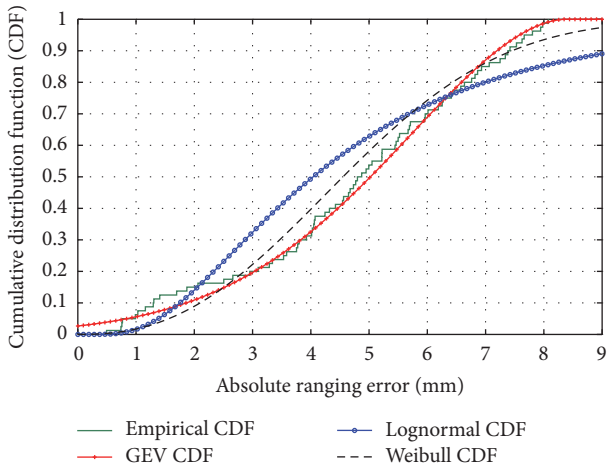

Figure 13: Comparison of the empirical CDF of ranging error with the GEV and lognormal and Weibull CDFs.

Another striking observation from Table 5 is the number of antenna depth values where the RMSE takes on values less than 1 mm. This suggests that it is possible to obtain range estimates with submillimeter accuracy, even in a challenging environment like the human body using NN techniques, as long as the NN structure is properly designed. The capability to obtain this level of accuracy in the range estimates can have profound implications for implant applications, such as next-generation microrobotic surgery or targeted drug delivery, where the location of the implant would be needed (so that the microrobot can be more precisely guided to the region where surgery is to be performed, e.g.).

On the basis of the results of Table 5, all further characterization of the ranging error was based only on the C-MLP structure, since it appears to exhibit the best (in terms of average RMSE) and most consistent (on the basis of the standard deviation of the RMSE) performance. As in the case of the CLEAN-based estimator, the same 9 candidate distributions were compared against the empirical distribution of the ranging error, using the A-D test. The results, again based on the p value, are shown in Table 6.

From the results of Table 6, we see that there are two alternative distributions to represent the ranging error statistics for the NN-based range estimator: the lognormal distribution and the GEV distribution. The Weibull distribution is also a possibility, although we see that the value of p is less than the significance level for the case of $d_0 = 60$ mm, indicating that the Weibull distribution does not represent the ranging error for this case. For all the other distributions, the values of p are observed to be less than the significance level for some or all implant depths. A closer inspection of the results for the GEV and lognormal distributions reveals that the p values for the GEV distribution are higher for most implant depths, making the GEV distribution the better choice. A

Table 5: Ranging RMSE for the three types of NN-based estimator.

Antenna depth (mm)	Ranging RMSE (mm)		
	Cascade-MLP (C-MLP)	MLP	Elman
40 mm	1,318	1,597	1,185
42 mm	0,682	0,610	0,757
44 mm	0,895	1,259	0,832
46 mm	0,864	1,912	1,337
48 mm	1,028	1,306	1,538
50 mm	0,805	1,065	0,640
52 mm	0,947	1,124	1,273
54 mm	0,881	0,626	0,568
56 mm	1,438	0,785	0,602
58 mm	0,484	0,792	0,537
60 mm	0,770	1,189	0,986
Average RMSE (mm)	*0,955*	*1,180*	*0,991*
Standard deviation of the RMSE (mm)	*0,270*	*0,405*	*0,360*

Table 6: The output of the A-D test (p values) as a function of d_0 for the C-MLP NN range estimator.

Distribution function	Antenna depth (mm)										
	40	42	44	46	48	50	52	54	56	58	60
Lognormal	0,72	0,28	0,28	0,19	0,32	0,77	0,07	0,18	0,41	0,21	0,09
Normal	0,00	0,06	0,02	0,00	0,00	0,00	0,00	0,01	0,00	0,00	0,00
GEV	0,96	0,73	0,33	0,57	0,41	0,73	0,64	0,92	0,91	0,66	0,65
Rayleigh	0,00	0,00	0,00	0,00	0,00	0,00	0,00	0,00	0,00	0,00	0,00
Weibull	0,09	0,96	0,77	0,95	0,16	0,84	0,58	0,59	0,73	0,25	0,01
Gamma	0,22	0,94	0,78	0,95	0,13	0,68	0,58	0,73	0,74	0,34	0,01
Exponential	0,01	0,15	0,82	0,49	0,12	0,31	0,50	0,10	0,73	0,11	0,00
Nakagami	0,01	0,72	0,67	0,35	0,00	0,08	0,21	0,16	0,18	0,03	0,00
Logistic	0,02	0,22	0,05	0,01	0,00	0,00	0,01	0,15	0,01	0,03	0,00

visual comparison of the CDFs of some of these candidate distributions against the empirical CDF of the ranging error is presented in Figure 14.

Finally, we present the parameter values for the GEV distribution as a function of the implant depth (d_0) in Table 7.

4.3. Discussion. On the basis of the results presented in Sections 4.1 and 4.2, a few final points are worthy of mention.

First, it is clear that the NN-based estimator outperforms the CLEAN-based estimator. This is evident from the RMSE figures presented in Tables 1 and 5. Indeed, for some implant depths, the NN-based estimator is capable of submillimeter ranging accuracy. Another quantitative comparison is provided by Figure 15, where the empirical CDFs of the ranging error for both the CLEAN-based and NN-based estimators are shown. It can be seen from the figure that the NN-based estimator can provide range estimates with an absolute ranging error of 3.23 mm or less with 90% probability, whereas the CLEAN-based estimator can provide an absolute ranging error performance of 5.634 mm or less with the same probability. This clearly indicates that the NN-based estimator can provide almost twice as good performance as the CLEAN-based estimator.

A possible explanation for this observation is that the CLEAN-based estimator relies on an accurate mathematical model of the relative permittivity, ε_r, as a function of the implant depth, d_0. It is possible that the limited accuracy of this model resulted in the relatively poor ranging performance of the CLEAN-based estimator. Making this model more accurate would be expected to improve the performance of this estimator. The NN-based range estimator,

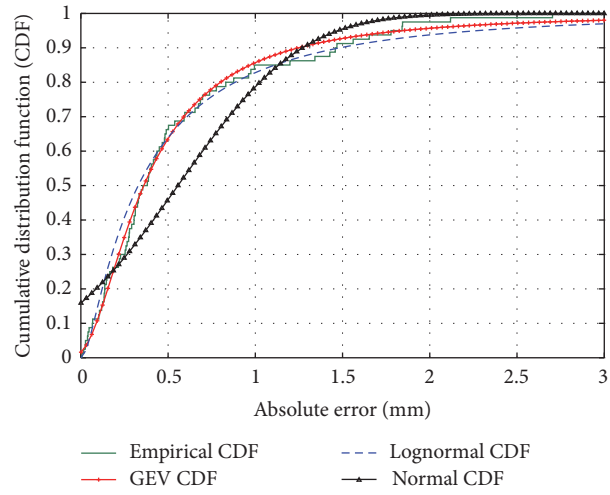

Figure 14: Comparison of the empirical CDF of the ranging error for the range estimator based on C-MLP NN, with other candidate distributions.

Table 7: GEV parameters as a function of the implant depth (d_0).

GEV parameters	Antenna depth (mm)										
	40	42	44	46	48	50	52	54	56	58	60
κ	0,31	0,23	0,49	0,62	0,59	0,71	0,46	0,25	0,46	0,32	0,56
σ	0,48	0,23	0,44	0,54	0,27	0,26	0,35	0,22	0,25	0,25	0,27
μ	0,70	0,28	0,43	0,48	0,28	0,24	0,34	0,27	0,26	0,30	0,51

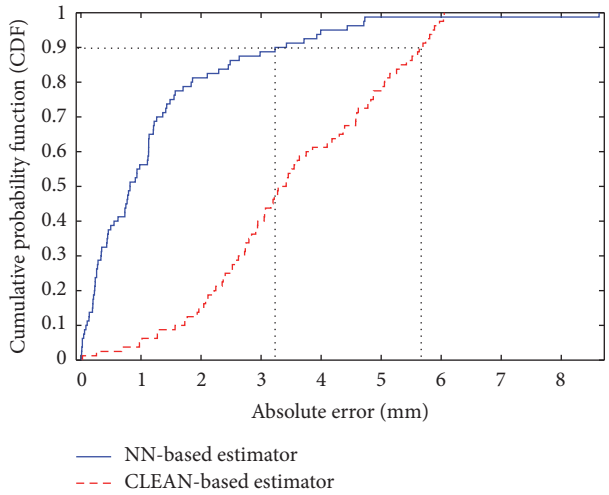

Figure 15: Cumulative CDFs of the ranging error for the NN-based and CLEAN-based range estimators (d_0 = 46 mm).

on the other hand, is a frequency-domain method which uses the Poynting vector magnitude information at different frequencies and different distances from the implant. As a result, the NN-based estimator avoids the possible ranging errors resulting from inaccurate estimation of ε_r. In a loose and purely qualitative sense, it can be said that the NN-based estimator takes into account the information on the frequency-dependent effects of the in-body channel, which is embedded in the whole spectrum of the received UWB signal, and leverages this information to come up with a more accurate estimate of the range.

It may be instructive to compare the results to other UWB-based range estimators operating in the in-body context. Unfortunately, in the course of our literature search, we were unable to find any other works except [27] dealing with UWB-based in-body ranging through maximum likelihood techniques that would allow a direct comparison. The results indicated in that study show a best-case ranging RMSE of about 23.5 mm. Based on the results presented in Sections 4.1 and 4.2, we observe that both the CLEAN-based estimator and the NN-based estimator outperform the maximum likelihood estimator.

Lastly, in the case of both the CLEAN-based estimator and the NN-based estimator, the ranging error statistics are well represented by the GEV distribution. The GEV distribution is commonly used to model certain statistical phenomena exhibiting heavy-tail behavior, such as extreme events in climatology, hydrology, and finance [47]. The GEV distribution has also been encountered in modeling the high amounts of ranging error due to shadowed undetected direct path (S-UDP) conditions for indoor localization [48]. Such heavy-tail phenomena are present in the in-body propagation environment as well. The body tissues attenuate and seriously distort the transmitted UWB signal in a frequency-selective way, and the scattering component of the path loss has been observed to be well represented by another heavy-tail distribution, namely, the Weibull distribution [19]. The DP component of the signal is likely to be highly obstructed owing to the lossy and nonhomogeneous nature of the human body environment. The presence of the GEV distribution for the in-body ranging error, therefore, is by no means a coincidence. Further studies in this area will no doubt allow greater understanding of the ranging problem within the human body, making high-accuracy in-body ranging and localization a reality.

5. Conclusions

In this paper, we focused on the problem of ranging with UWB signals in the in-body environment and proposed two range estimators to address this problem: one based on an implementation of the CLEAN algorithm and another based on neural network (NN) techniques. The performance of both estimators was analyzed in a systematic manner. The results clearly indicate that the NN-based estimator outperforms the CLEAN-based estimator, with submillimeter-scale ranging accuracy for some cases. The ranging error resulting from both estimators was observed to exhibit heavy-tail behavior and found to be well represented by a Generalized Extreme Value (GEV) distribution. The results shed light on fundamental issues surrounding ranging and localization for the in-body environment.

Competing Interests

The authors declare that there is no conflict of interests regarding the publication of this paper.

Acknowledgments

This work was supported by the Erciyes University Research Projects Fund under Grant no. FYL-2014-5429.

References

[1] H.-B. Li, K. Y. Yazdandoost, and B. Zhen, *Wireless Body Area Network*, River, Aalborg, Denmark, 2010.

[2] P. C. Swain, "Wireless capsule endoscopy," *Gut*, vol. 52, no. 4, pp. iv48–iv50, 2003.

[3] K. Pahlavan, G. Bao, Y. Ye et al., "RF localization for wireless video capsule endoscopy," *International Journal of Wireless Information Networks*, vol. 19, no. 4, pp. 326–340, 2012.

[4] K. Pahlavan and A. H. Levesque, *Wireless Information Networks*, John Wiley & Sons, Hoboken, NJ, USA, 2nd edition, 2005.

[5] R. Chávez-Santiago and I. Balasingham, "Computation of the transmission frequency band for the ultra wideband capsule endoscope," in *Proceedings of the 7th International Symposium on Medical Information and Communication Technology (ISMICT '13)*, pp. 66–70, Tokyo, Japan, March 2013.

[6] A. Khaleghi, R. Chávez-Santiago, and I. Balasingham, "Ultra-wideband pulse-based data communications for medical implants," *IET Communications*, vol. 4, no. 15, pp. 1889–1897, 2010.

[7] M. R. Yuce, H. C. Keong, and M. S. Chae, "Wideband communication for implantable and wearable systems," *IEEE Transactions on Microwave Theory and Techniques*, vol. 57, no. 10, pp. 2597–2604, 2009.

[8] D. Dardari, A. Conti, U. Ferner, A. Giorgetti, and M. Z. Win, "Ranging with ultrawide bandwidth signals in multipath environments," *Proceedings of the IEEE*, vol. 97, no. 2, pp. 404–426, 2009.

[9] J. A. Högbom, "Aperture synthesis with a non-regular distribution of interferometer baselines," *Astronomy and Astrophysics Supplement*, vol. 15, pp. 417–426, 1974.

[10] C. Gabriel, "Compilation of the dielectric properties of body tissues at RF and microwave frequencies," Tech. Rep. AL/OE-TR-1996-000, Brooks Air Force, San Antonio, Tex, USA, 1996, http://www.dtic.mil/cgi-bin/GetTRDoc?AD=ADA303903.

[11] D. Anzai, K. Katsu, R. Chávez-Santiago et al., "Experimental evaluation of implant UWB-IR transmission with living animal for body area networks," *IEEE Transactions on Microwave Theory and Techniques*, vol. 62, no. 1, pp. 183–192, 2014.

[12] H. Bahrami, B. Gosselin, and L. A. Rusch, "Realistic modeling of the biological channel for the design of implantable wireless UWB communication systems," in *Proceedings of the Annual International Conference of the IEEE Engineering in Medicine and Biology Society (EMBC '12)*, vol. 2, pp. 6015–6018, September 2012.

[13] V. De Santis and M. Feliziani, "Intra-body channel characterization of medical implant devices," in *Proceedings of the EMC Europe*, pp. 816–819, York, UK, September 2011.

[14] R. Chávez-Santiago, K. Sayrafian-Pour, A. Khaleghi et al., "Propagation models for IEEE 802.15.6 standardization of implant communication in body area networks," *IEEE Communications Magazine*, vol. 51, no. 8, pp. 80–87, 2013.

[15] A. Khaleghi, R. Chávez-Santiago, and I. Balasingham, "An improved ultra wideband channel model including the frequency-dependent attenuation for in-body communications," in *Proceedings of the Annual International Conference of the IEEE Engineering in Medicine and Biology Society (EMBC '12)*, pp. 1631–1634, August-September 2012.

[16] S. Støa, R. Chávez-Santiago, and I. Balasingham, "An ultra wideband communication channel model for the human abdominal region," in *Proceedings of the IEEE GLOBECOM Workshops (GC Wkshps '10)*, pp. 246–250, December 2010.

[17] M. Cavagnaro, E. Pittella, and S. Pisa, "UWB pulse propagation into human tissues," *Physics in Medicine and Biology*, vol. 58, no. 24, pp. 8689–8707, 2013.

[18] G. Varotto and E. M. Staderini, "On the UWB medical radars working principles," *International Journal of Ultra Wideband Communications and Systems*, vol. 2, no. 2, pp. 83–93, 2011.

[19] M. Kanaan and M. Suveren, "A novel frequency-dependent path loss model for ultra wideband implant body area networks," *Measurement*, vol. 68, pp. 117–127, 2015.

[20] Y. Kiliç, A. J. Ali, A. Meijerink, M. J. Bentum, and W. G. Scanlon, "The effect of human-body shadowing on indoor UWB TOA-based ranging systems," in *Proceedings of the 9th Workshop on Positioning, Navigation and Communication (WPNC '12)*, pp. 126–130, Dresden, Germany, March 2012.

[21] J. Hamie, B. Denis, R. D'Errico, and C. Richard, "On-body TOA-based ranging error model for motion capture applications within wearable UWB networks," *Journal of Ambient Intelligence and Humanized Computing*, vol. 6, no. 5, pp. 603–612, 2015.

[22] Y. Geng, J. He, and K. Pahlavan, "Modeling the effect of human body on TOA based indoor human tracking," *International Journal of Wireless Information Networks*, vol. 20, no. 4, pp. 306–317, 2013.

[23] J. He, Y. Geng, and K. Pahlavan, "Toward accurate human tracking: modeling time-of-arrival for wireless wearable sensors in multipath environment," *IEEE Sensors Journal*, vol. 14, no. 11, pp. 3996–4006, 2014.

[24] Y. Ye, K. Pahlavan, G. Bao, P. Swar, and K. Ghaboosi, "Comparative performance evaluation of RF localization for wireless capsule endoscopy applications," *International Journal of Wireless Information Networks*, vol. 21, no. 3, pp. 208–222, 2014.

[25] J. Chen, Y. Ye, and K. Pahlavan, "Comparison of UWB and NB RF ranging measurements in homogenous tissue for BAN applications," in *Proceedings of the 12th Annual Wireless Telecommunications Symposium (WTS '13)*, pp. 1–5, Phoenix, Ariz, USA, April 2013.

[26] J. Chen, *UWB characteristics of RF propagation for body mounted and implanted sensors [M.S. thesis]*, Worcester Polytechnic Institute, Worcester, Mass, USA, 2013.

[27] M. Kanaan, "Ranging based on maximum likelihood techniques for ultra wideband medical implants," in *Proceedings of the 2011 IEEE 22nd International Symposium on Personal, Indoor and Mobile Radio Communications (PIMRC '11)*, pp. 2234–2238, Ontario, Canada, September 2011.

[28] R. J.-M. Cramer, R. A. Scholtz, and M. Z. Win, "Evaluation of an ultra-wide-band propagation channel," *IEEE Transactions on Antennas and Propagation*, vol. 50, no. 5, pp. 561–570, 2002.

[29] A. Khaleghi, R. Chávez-Santiago, X. Liang, I. Balasingham, V. C. M. Leung, and T. A. Ramstad, "On ultra wideband channel modeling for in-body communications," in *Proceedings of the 5th IEEE International Symposium on Wireless Pervasive Computing (ISWPC '10)*, pp. 140–145, Modena, Italy, May 2010.

[30] B. S. Shin, "Reconstruction of human anatomical models from segmented contour lines," *Computational and Information Science*, vol. 3314, pp. 619–624, 2004.

[31] J.-Y. Lee and R. A. Scholtz, "Ranging in a dense multipath environment using an UWB radio link," *IEEE Journal on Selected Areas in Communications*, vol. 20, no. 9, pp. 1677–1683, 2002.

[32] F. Shang, B. Champagne, and I. Psaromiligkos, "Time of arrival and power delay profile estimation for IR-UWB systems," *Signal Processing*, vol. 93, no. 5, pp. 1317–1327, 2013.

[33] N. A. Alsindi, B. Alavi, and K. Pahlavan, "Measurement and modeling of ultrawideband TOA-based ranging in indoor multipath environments," *IEEE Transactions on Vehicular Technology*, vol. 58, no. 3, pp. 1046–1058, 2009.

[34] S.-H. Fang and T.-N. Lin, "Indoor location system based on discriminant-adaptive neural network in IEEE 802.11 environments," *IEEE Transactions on Neural Networks*, vol. 19, no. 11, pp. 1973–1978, 2008.

[35] M. S. Rahman, Y. Park, and K.-D. Kim, "RSS-based indoor localization algorithm for wireless sensor network using generalized regression neural network," *Arabian Journal for Science and Engineering*, vol. 37, no. 4, pp. 1043–1053, 2012.

[36] J. Xu, H. Dai, and W. Ying, "Multi-layer neural network for received signal strength-based indoor localisation," *IET Communications*, vol. 10, no. 6, pp. 717–723, 2016.

[37] J. H. Lee, S. J. Lee, Y. Park, K. B. Yun, and K. D. Kim, "RSS based indoor localization scheme using GRNN and virtual grid-points," *International Journal of Advanced Research in Electrical, Electronics and Instrumentation Engineering*, vol. 1, pp. 478–486, 2012.

[38] Remcom, http://www.remcom.com/xf7.

[39] A. Khaleghi and I. Balasingham, "Improving in-body ultra wideband communication using near-field coupling of the implanted antenna," *Microwave and Optical Technology Letters*, vol. 51, no. 3, pp. 585–589, 2009.

[40] Q. Wang, K. Masami, and J. Wang, "Channel modeling and BER performance for wearable and implant UWB body area links on chest," in *Proceedings of the IEEE International Conference on Ultra-Wideband (ICUWB '09)*, pp. 316–320, IEEE, Vancouver, Canada, September 2009.

[41] J. Wang and Q. Wang, *Body Area Communications: Channel Modeling, Communication Systems and EMC*, John Wiley & Sons, Singapore, 2013.

[42] J. L. Elman, "Finding structure in time," *Cognitive Science*, vol. 14, no. 2, pp. 179–211, 1990.

[43] A. Muqaibel, A. Safaai-Jazi, A. Bayram, A. M. Attiya, and S. M. Riad, "Ultrawideband through-the-wall propagation," *IEE Proceedings Microwaves, Antennas and Propagation*, vol. 152, no. 6, pp. 581–588, 2005.

[44] C.-F. Yang, C.-J. Ko, and B.-C. Wu, "A free space approach for extracting the equivalent dielectric constants of the walls in buildings," in *Proceedings of the AP-S. Digest Antennas and Propagation Society International Symposium*, pp. 1036–1039, July 1996.

[45] N. M. Razali and Y. B. Wah, "Power comparisons of shapiro-wilk, kolmogorov-smirnov, lilliefors and anderson-darling tests," *Journal of Statistical Modeling and Analytics*, vol. 2, no. 1, pp. 21–33, 2011.

[46] MATLAB R2013a Documentation, "Anderson-Darling Test," 2013.

[47] S. Markose and A. Alentorn, The Generalized Extreme Value (GEV) Distribution, Implied Tail Index and Option Pricing, Economics Discussion Papers 594, Univer-sity of Essex, Department of Economics, 2005, http://repository.essex.ac.uk/3726/1/dp594.pdf.

[48] M. Heidari, *Identification and modeling of the dynamic behavior of the direct path component in ToA-based indoor localization systems [Ph.D. dissertation]*, Worcester Polytechnic Institute, 2008.